Modeling and Control of an Aeroelastic Morphing Vehicle

Dario H. Baldelli* and Dong-Hwan Lee†
ZONA Technology, Inc., Scottsdale, Arizona 85258
Ricardo S. Sánchez Peña‡
Universitat Politècnica de Catalunya, 08222 Barcelona, Spain
and
Bryan Cannon§
U.S. Air Force Research Laboratory, Wright–Patterson Air Force Base, Ohio, 45443

Morphing aircraft are conceived as multirole platforms that modify their external shape substantially to adapt to a changing mission environment. The dynamic response of the unmanned aerial vehicle will be governed by the time-varying aerodynamic forces and moments which will be a function of the wing's shape changes by the morphing command. Here, it is assumed that the morphing unmanned aerial vehicle behaves as a variable geometry rigid body, but with dynamic coefficients corrected to include quasi-steady aeroelastic effects. A multiloop controller for the aeroelastic morphing unmanned aerial vehicle concept is formulated to provide both proven structural and self-scheduled characteristics. The proposed controller uses a set of inner-loop gains to provide stability using classical techniques, whereas a linear parameter-varying outer-loop controller is devised to guarantee a specific level of robust stability and performance for the time-varying dynamics. Reduced-order controllers are synthesized using a robust control reduction technique. A series of maneuvers are devised to exhaustively evaluate the performance of the synthesized multiloop controller subject to large-scale geometrical shape changes. The underlying multiloop approach successfully enables in-flight transformation between vehicle states in less than one minute, while maintaining the overall vehicle stability and control.

I. Introduction

ONGOING research activities focus on designing novel wing concept technologies for future unmanned aerial vehicles (UAVs) and several innovative aircraft designs that have appeared as part of the Defense Advanced Research Projects Agency/U.S. Air Force Morphing Aircraft Structures program.

One of these designs uses an evolutionary folding-wing scheme to adjust flight performance from an efficient cruise configuration to an efficient high-speed dash configuration. This folding-wing scheme, known as the out-of-plane or Z-wing design is achieved by morphing into a fuselage conformal configuration for attack or rapid evasive maneuvers [1]. Figure 1 schematically shows this morphing concept.

In general, any morphing approach will involve large rigid-body motions of the UAV's flexible structure under aerodynamic and distributed actuation system loads. In that scenario, the response of the UAV will be governed by the time-varying aerodynamic forces and moments which will be a function of the wing's shape changes by the morphing command.

Dynamic models for the morphing UAV must properly take into account its inherent time-varying nature due to the dynamic coupling between inertial (wing's area and mass distribution changes),

aerodynamics, structural, and distributed control forces. Unfortunately, such a complex dynamic behavior is obviously quite difficult to analyze theoretically. In such cases, no reasonable or unique set of model equations are available to the control engineer. One possible approach is to assume that the time-varying dynamics could be represented by a linear parameter-varying (LPV) plant model that approximately captures the morphing UAV's complex behavior. In this LPV framework, the system dynamics will be modeled using a set of state-space models with the coefficient matrices function of a morphing scheduling parameter vector $\sigma(t)$ [2].

A multiloop controller for the aeroelastic morphing UAV concept is formulated to provide both proven structural and self-scheduled characteristics. The proposed controller uses a set of inner-loop gains to provide stability and some level of performance to the morphing UAV dynamics, whereas an outer-loop LPV controller is devised to guarantee a specific level of robust stability and performance. The system LPV's poles¶ are satisfactorily located in a region of the complex plane using the proposed LPV technique with pole placement constraints.

In this work, reduced-order controllers are synthesized for the aeroelastic morphing UAV concept using a robust control reduction technique. The reduction was executed on the higher-order outer-loop LPV controller. Simulation studies were performed on several meaningful time-varying controlled case studies to validate the proposed control algorithms. It was found that the underlying multiloop approach successfully enables in-flight large-scale geometrical shape changes in less than 1 min, while maintaining the overall vehicle stability and control.

This paper is organized as follows. The next section describes the morphing UAV dynamics as an LPV model and its simplification through the small convex hull approach to reduce computations for controller design. The approach adopted in this work closely follows the framework developed by Kumar and Anderson [3]. Section III describes the classical inner and LPV outer loops of the controller, and Sec. IV describes its model order reduction in case it is needed for real-time implementation. The time response of the closed-loop

*Research and Development Control Manager in ZONA Technology; currently Associate Technical Fellow at Northrop Grumman Corporation, Vehicle Management System, Guidance, Navigation & Control. AIAA Senior Member.

†Structural Engineering Specialist. AIAA Member.

‡Research Professor, Institucio Catalana de Recerca i Estudis Avancats. AIAA Senior Member.

§Research Aerospace Engineer, Control Systems Development and Applications Branch. AIAA Member.

¶Actually, these are denoted as "frozen" poles, because they are fixed time closed-loop poles, due to the fact that these are time-varying models.

Fig. 1 Evolutionary out-of-plane morphing UAV concept [1].

system for several morphing maneuvers are simulated in Sec. V, for both the full- and reduced-order controllers. Final conclusions close the paper in Sec. VI.

II. Aeroelastic Morphing Dynamics: Linear Parameter-Varying Model

Lets consider the three degree-of-freedom nonlinear body-fixed equations of motion that result from the morphing UAV's longitudinal dynamics,

$$\dot{u} = \frac{F_x}{m} - \frac{\dot{m}u}{m} - qw - g\sin\theta$$

$$\dot{w} = \frac{F_z}{m} - \frac{\dot{m}w}{m} + qu - g\cos\theta \qquad \dot{q} = \frac{M_y}{I_y} - \frac{\dot{I}_y q}{I_y} \tag{1}$$

with $\dot{\theta} = q$. Here, $u(t)$, $w(t)$, $q(t)$, and $\theta(t)$ are the *perturbed* forward speed, vertical speed, pitch rate, and pitch angle of the UAV. Additionally, m, I_y, $\dot{m}$, and $\dot{I}_y$ are the morphing UAV's mass, moment of inertia, and their respective rate of change. This set of equations describes the short-period dynamics at trimmed level flight, as well as at trimmed and symmetric climbing flight in the vertical plane. Both flight conditions will be considered throughout this work.

The aerodynamic forces and pitching moment are produced by the elastic UAV's relative motion with respect to the air flow and are proportional to the dynamic pressure q_∞. In addition, they are determined by the angle of attack $\alpha(t)$ with respect to the relative wind. In this work, it is assumed that the morphing UAV behaves as a variable geometry rigid body, but the dynamic coefficients used in the differential equations are corrected for static aeroelastic effects.

Generally, $F_x(t)$, $F_z(t)$, and $M_y(t)$ are expressed as a function of the main variables that govern the motion by a Taylor series. Dividing the force equations by the mass m, and the moment equation by the moment of inertia I_y, allowing them to be expressed in terms of the dimensional stability and control derivatives [4],

$$\frac{F_x}{m} = X_u u + X_q q + X_w w + X_{\dot{w}}\dot{w} + X_{\delta_e}\delta_e + X_{\text{dist}}\delta_{\text{dist}}$$

$$\frac{F_z}{m} = Z_u u + Z_q q + Z_w w + Z_{\dot{w}}\dot{w} + Z_{\delta_e}\delta_e + Z_{\text{dist}}\delta_{\text{dist}} \tag{2}$$

$$\frac{M_y}{I_y} = M_u u + M_q q + M_w w + M_{\dot{w}}\dot{w} + M_{\delta_e}\delta_e + M_{\text{dist}}\delta_{\text{dist}}$$

where X_i, Z_i, and M_i, $i = u, q, w, \dot{w}, \delta_e, \delta_{\text{dist}}$, are the dimensional aeroelastic stability derivatives related with the drag force, lift force, and pitch moment changes due to increases in forward speed $u(t)$, pitching rate $q(t)$, vertical speed along the Z axis $w(t)$, its rate of change $\dot{w}(t)$, control surface deflection (traditional) $\delta_e(t)$, and distributed actuation system $\delta_{\text{dist}}(t)$, respectively.

This setup allows the modeling of an integrated morphing wing control environment throughout both variables $\delta_e(t)$ and $\delta_{\text{dist}}(t)$. Specifically, if only traditional control effectors, such as electromechanical elevators, are sought to provide stability and control, then $\delta_e(t)$ becomes the input control variable for the LPV system. Otherwise, when a distributed control environment is considered to perform the same task using smart-material actuators, the $\delta_{\text{dist}}(t)$ variable must be selected.

Clearly, any of those dimensional stability derivatives will be very much affected by out-of-plane morphing changes. For example, considering the change in pitch moment due to an increase of the vertical speed along the Z axis, that is, M_w,

$$M_w = \frac{q_\infty S\bar{c}}{I_y U_0} C_{m_\alpha} \tag{3}$$

where $q_\infty = 0.5\rho_{\text{air}}U_0^2$, S, $\bar{c}$, I_y, and C_{m_α} are the dynamic pressure, the wing area, and aerodynamic mean chord, the UAV's moment of inertia around the pitch axis, and the nondimensional "pitch stiffness" (C_{m_α}) aerodynamic stability derivative.

Similar to the analysis of a conventional aircraft, the mass of the morphing UAV is assumed to remain constant, then $\dot{m} = 0$ in Eqs. (1) for the duration of any particular dynamic analysis, but all similarities stop there. Now, in addition to the presumably nonlinear behavior of the nondimensional aeroelastic aerodynamic stability derivative throughout the range of Mach number, dynamic pressure, and morphing configuration variable $\chi(t)$, for instance, $C_{m_\alpha} = C_{m_\alpha}(M, q_\infty, \chi)$, the wing's aspect ratio and mass distribution might also become functions of the morphing strategy. The former will give rise to a time-varying UAV's moment of inertia $I_y(t)$ and wing area $S(t)$. As expected, in usual flutter engineering modeling practice, it was assumed that the variations in the moment of inertia due to elastic deformation are small and hence neglected. The moment of inertia actually used in the equations of motion correspond to the undeformed vehicle at each specific morphing configuration given by the parameter $\chi(t)$. Hence, all coupling between rigid-body motion and structural deformation will occur by means of the quasi-steady corrected aerodynamics coefficients.

Based on Eqs. (1) and (2), an LPV model can be generated for some specified mission profile,

$$\begin{bmatrix} \dot{x}_\delta \\ z_\delta \\ y_\delta \end{bmatrix} = \begin{bmatrix} A(\sigma) & B_1(\sigma) & B_2(\sigma) \\ C_1(\sigma) & D_{11}(\sigma) & D_{12}(\sigma) \\ C_2(\sigma) & D_{21}(\sigma) & 0 \end{bmatrix} \begin{bmatrix} x_\delta \\ w_\delta \\ u_\delta \end{bmatrix} \tag{4}$$

or in compact form,

$$\begin{bmatrix} \dot{x}_\delta \\ z_\delta \\ y_\delta \end{bmatrix} = \begin{bmatrix} A(\sigma) & B(\sigma) \\ C(\sigma) & D(\sigma) \end{bmatrix} \begin{bmatrix} x_\delta \\ w_\delta \\ u_\delta \end{bmatrix} \tag{5}$$

where A, B, C, D are continuous and possibly nonlinear matrix values functions of the vector of scheduling variables $\sigma(t)$, to be defined in the ensuing sections.

Figure 2 schematically depicts the state-space LPV model. The design procedure of the LPV controller $K(\sigma)$ is provided in Sec. III. To this end, the time-varying aerodynamic forces and moments, due to rigid-body motions of the generally flexible morphing UAV under
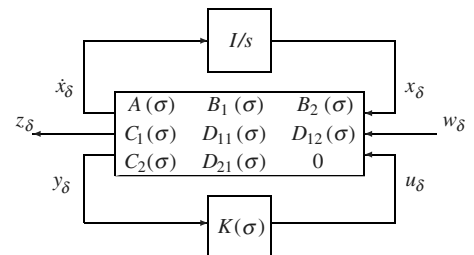

Fig. 2 State-space parameter-dependent LPV representation.

large-scale shape changes, will be approximated at a discrete set of flight conditions using a linear flutter engineering tool [5].

A. Modeling of the Morphing UAV: Linear Parameter-Varying Model Generation

From an aerodynamic viewpoint, there are fundamentally two time scales: one for the rate of change of the wing shape, and the other for the unsteady motion of the aircraft through the dynamic variables, such as $\dot\alpha$, $\dot\beta$, etc. A practical consideration that simplifies the analysis is based on the assumption that the in-plane and/or out-of-plane morphing shape change is slow varying, between 30 s and 1 min. Then, the unsteady aerodynamic effects that resulted due to the wing shape's change of rate can be ignored, that is, $X_{\dot w} = Z_{\dot w} = M_{\dot w} \equiv 0$.

To build the morphing aeroelastic LPV system, an intensive computational effort was performed. A set of linear time-invariant (LTI) models were generated at N operating points, which are composed of n_f flight conditions and c_m morphing elastic configurations, that is, $N = n_f \times c_m$. This building process is schematically represented by Fig. 3. The overall LPV modeling strategy to design a *practical* LPV flight controller is explained in next subsection. Briefly, a set of parameters $\{\sigma_i\}_{i=1,N}$, one for each flight condition, defines a multimodel set and is used to schedule the LPV model. In turn, each parameter is related to a particular vector of aeroelastic coefficients ρ_i, taking into consideration the trimming condition. The whole idea is to sensibly reduce the total number of parameter vertices N, each related to an LTI model, to attain a practical affine LPV model which can be described *exclusively* by the vertex values σ_i. The affine LPV model can be scheduled by $\sigma(t)$, which is a convex combination of these vertices σ_i.

The outcome of this modeling process are N sets of dimensional aeroelastic stability derivatives upon which the morphing LPV models are generated. Five structural models with different inboard wing folding angles were employed, that is, $\chi = 0, 45, 65, 90$, and 125 deg. As an example, the first four mode shapes of the morphing UAV for $\chi = 65$ deg are displayed in Fig. 4.

For this modeling process, the flight condition parameters are 1) Mach numbers $M = 0.5, 0.6, 0.7, 0.8, 0.85, 0.9$, and 0.95; 2) altitude H varying from 5 to 50 kft with discrete increments, each 5 kft; and 3) wing folding angle $\chi = 0, 45, 65, 90$, and 125 deg.

a) First mode

b) Second mode
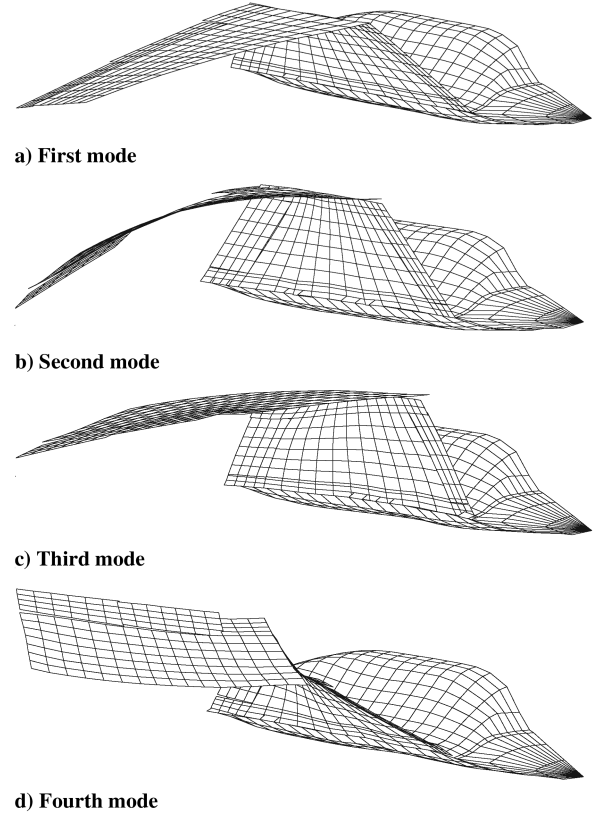
c) Third mode

d) Fourth mode

Fig. 4 First four elastic modes of the morphing UAV at $\chi = 65$ deg.

In this way, a total of 350 operating points are generated, that is, 70 flight conditions for each one of the wing folding angles. This set of dimensional aeroelastic derivatives form the coefficients of the differential equations that will describe the motion of the morphing UAV. A set of dimensional stability and control derivatives for the morphing UAV model are depicted through surface response plots in Figs. 5–7.
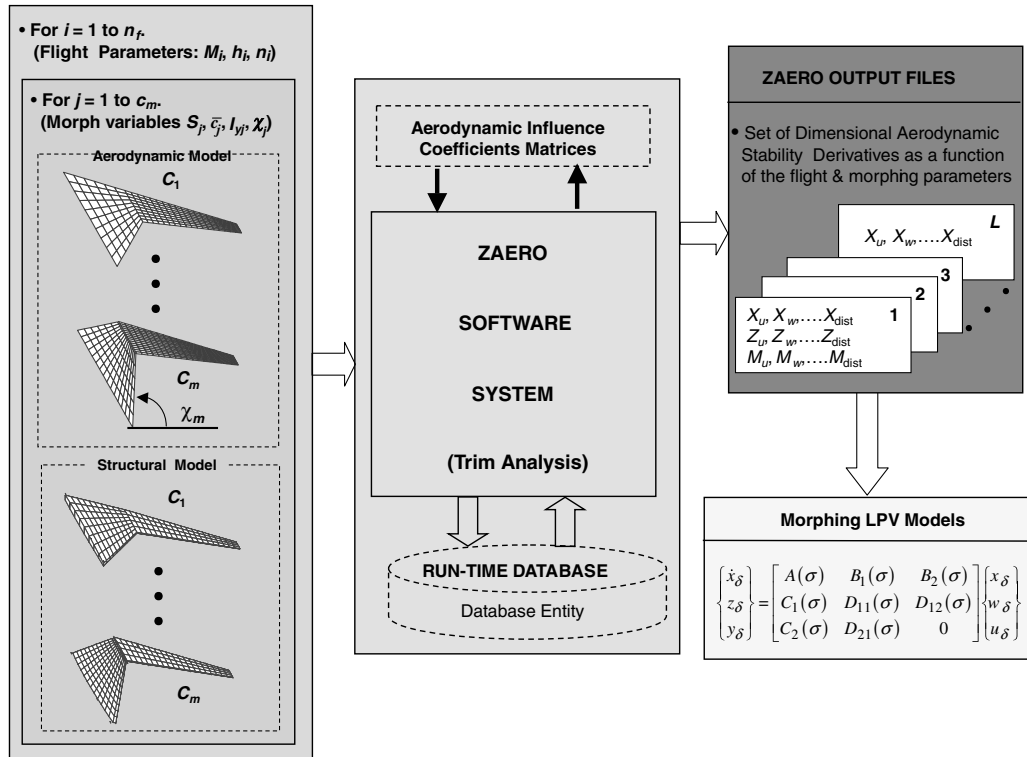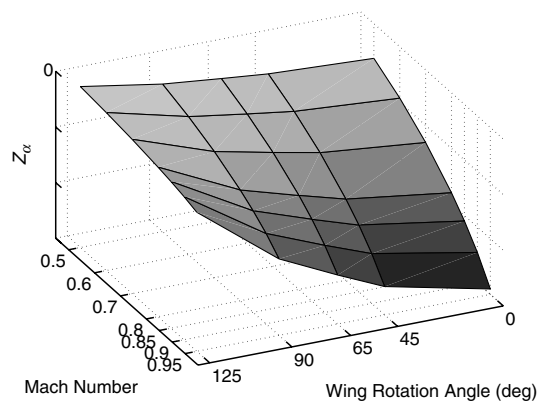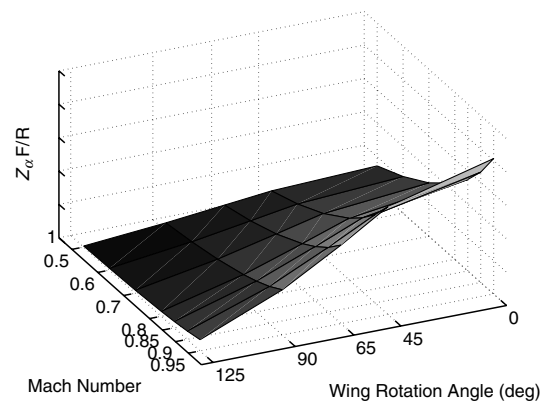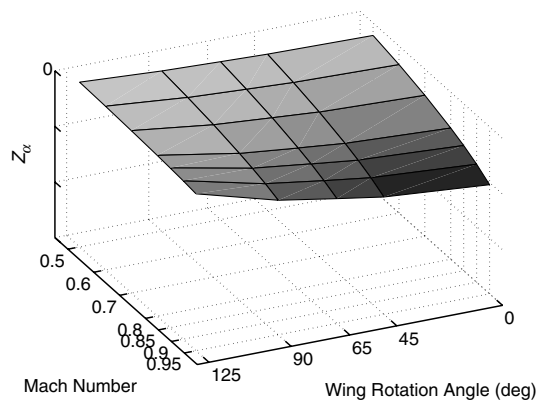

Fig. 3 Aeroelastic morphing LPV model generation.

a) Z_α at H = 5 kft
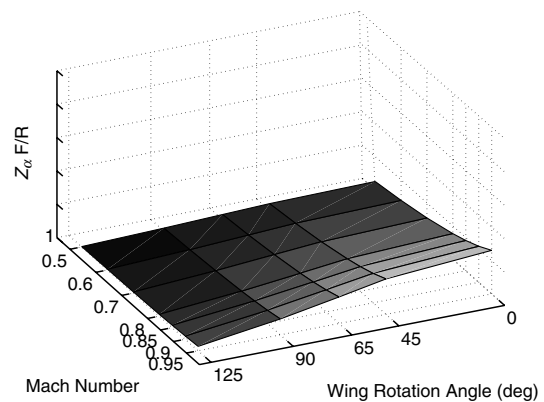
b) Flexible-to-rigid ratio at H = 5 kft

c) Z_α at H = 30 kft

d) Flexible-to-rigid ratio at H = 30 kft

e) M_α at H = 5 kft
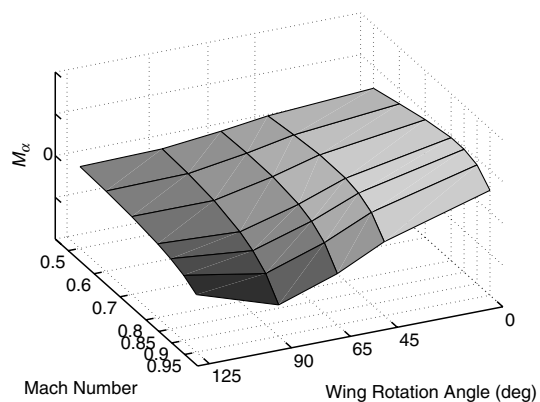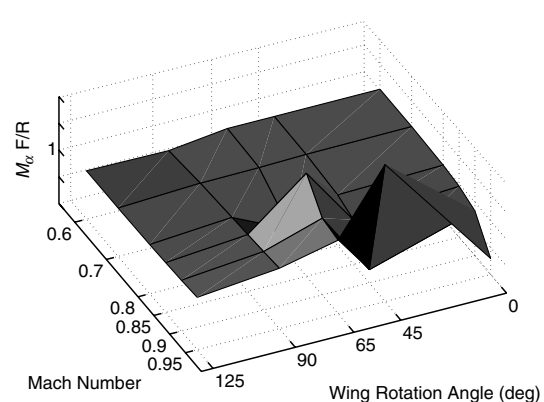
f) Flexible-to-rigid ratio at H = 5 kft
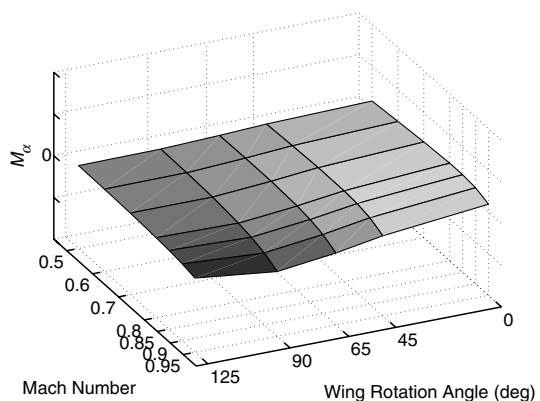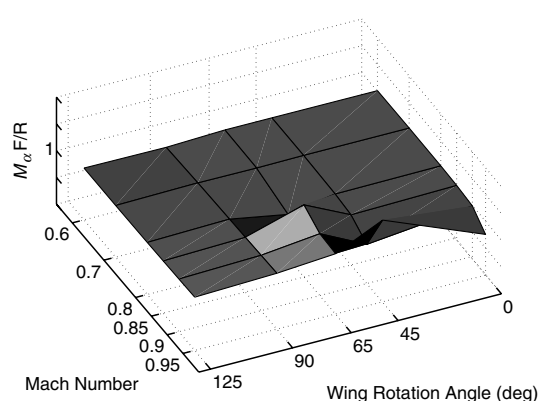
g) M_α at H = 30 kft

h) Flexible-to-rigid ratio at H = 30 kft

Fig. 5   Static aeroelastic dimensional stability derivatives Z_α and M_α as a function of the Mach number and wing rotation angle χ.

a) M_q at $H = 5$ kft

b) Flexible-to-rigid ratio at $H = 5$ kft

c) M_q at $H = 30$ kft

d) Flexible-to-rigid ratio at $H = 30$ kft
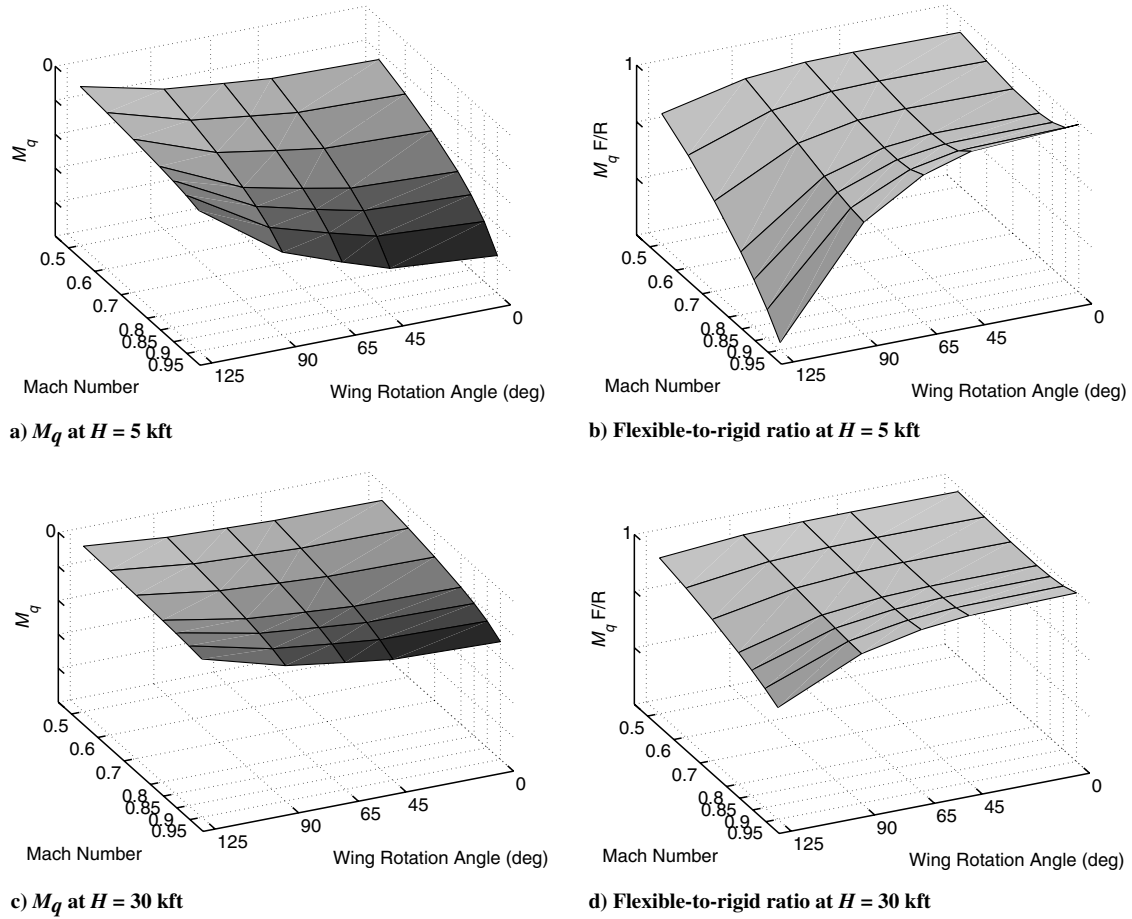
Fig. 6 Static aeroelastic dimensional stability M_q as a function of the Mach number and wing rotation angle χ.

As an example, the Z_α stability derivative corrected by quasi-steady aeroelastic effects in conjunction with its flexible-to-rigid ratio is shown through surface response plots in Fig. 5 at two different altitudes, that is, $H = 5$ and 30 kft. The last figure, Fig. 5d, indicates the effects of structural flexibility on the stability derivative. Note that a flexible-to-rigid ratio difference of one means that the static aeroelastic effects become important. As expected, these effects are more visible at lower altitudes (as seen in Fig. 5b) and must be taken into account during the flight control system synthesis stage.

From a behavioral point of view, two groups of dimensional aeroelastic derivatives were observed during this work. The first group, depicted in Figs. 5 and 6, involving the aeroelastic static stability derivatives, that is, Z_α, M_α, and M_q, presents a larger gradient variation with respect to the independent variables M and χ, as well as the influence of altitude on the plotted data for the fully extended configuration ($\chi = 0$ deg) when compared with the fully morphed configuration ($\chi = 125$ deg). In addition, the morphing UAV presents a static unstable behavior due to the positive values of M_α along several portions of the computed parameter space.

On the contrary, the second group, shown in Fig. 7, composed by the aeroelastic control derivatives Z_δ and M_δ, presents a smoother gradient variation with respect to the independent variables M and χ. Based on this observation, the control derivatives Z_δ and M_δ can be considered as constant parameters rather than varying ones. Therefore, the dimension of the vectors that result from stacking the aeroelastic derivatives, $\rho = [Z_\alpha \quad M_\alpha \quad \cdots \quad M_\delta]$, can be reduced and the LPV controller dimensional complexity is considerably decreased during the synthesis stage.

B. Convex Modeling Approach: Small Convex Hull Computation and Design Models Selection

The design procedure produces an LPV controller based on the set of extreme models derived from the set of flight operating conditions

$\{\sigma_i\}_{i=1,N}$. There are two different sets of models that can be generated:

1) The ones based on the set of aerodynamic parameters that can move inside certain intervals according to the flight conditions are denominated as the affine hull. In this case, five parameters Z_α Z_δ, M_α M_q, and M_δ produce 32 vertices, $\{\rho_i\}_{i=1,32}$. This affine hull actually includes an undetermined number of unfeasible flight conditions, presumably rendering more conservative results, that is, less performance.

2) The ones derived directly from the flight conditions $\{\sigma_i\}_{i=1,N}$, produced at different Mach numbers, altitudes, and wing folding angles, are called the small convex hull. Using the Q-hull software,** the number of extreme points, which define the convex hull and the size of the set of feasible operating conditions, can be drastically reduced.

One of the key issues to successfully design a practical flight controller is to reduce the conservatism of the morphing UAV's LPV model. Then, the reduction on conservatism is planned to be reached by applying the small convex hull approach on the parameter variation set $\sigma(t)$.

The small convex hull algorithm is a computational tool that can be applied to geometric spaces generated from state-space matrices. A matrix polytope is defined as the convex (Co) hull of a finite number of matrices T_i with the same dimensions, that is,

$$\text{Co}\{T_i, i = 1, \ldots, N\} := \left\{ \sum_{i=1}^{N} \gamma_i T_i : \gamma_i \geq 0, \sum_{i=1}^{N} \gamma_i = 1 \right\} \quad (6)$$

Now, if the parameter vector $\sigma(t)$ takes values within a geometric (convex) shape with corners $\{\sigma_i\}_{i=1,N}$, the LPV model as expressed by Eq. (5) can be defined as

---

**QuickHull algorithm, www.qhull.org.
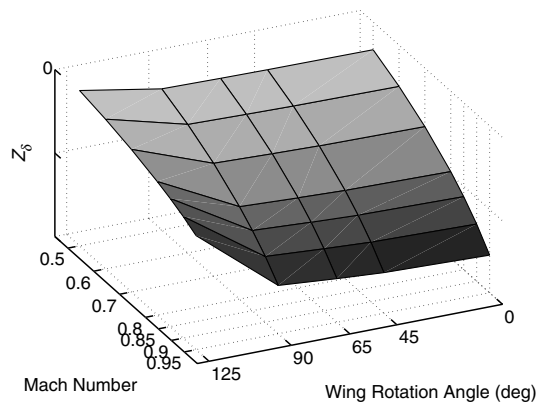
a) Z_δ at $H = 5$ kft
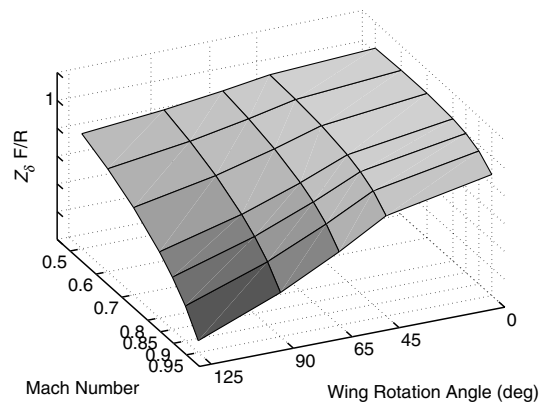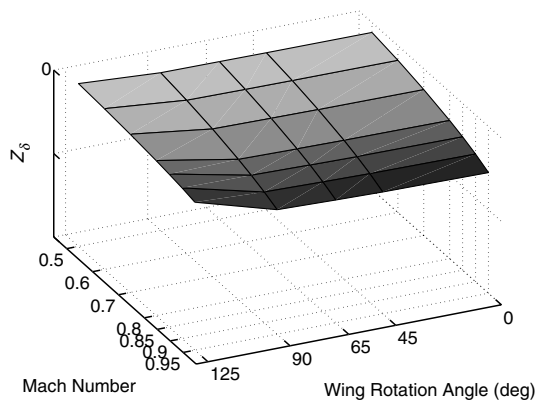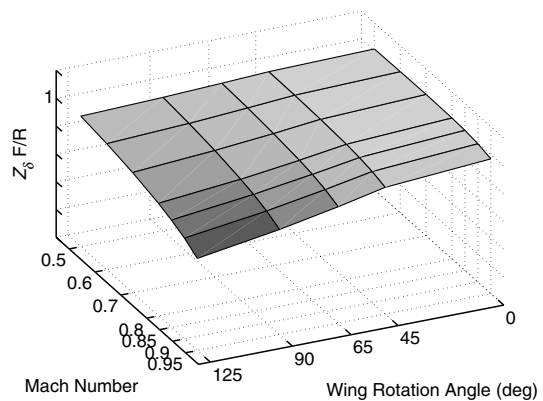
b) Flexible-to-rigid ratio at $H = 5$ kft

c) Z_δ at $H = 30$ kft

d) Flexible-to-rigid ratio at $H = 30$ kft

e) M_δ at $H = 5$ kft
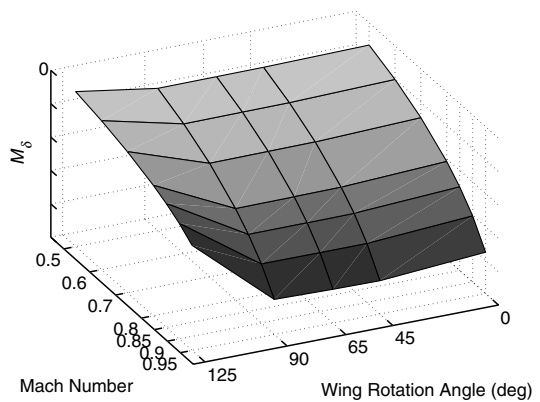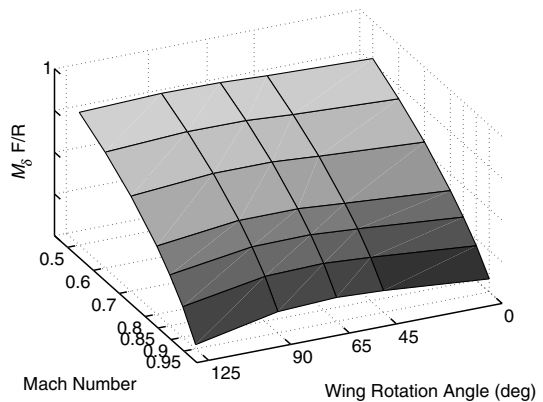
f) Flexible-to-rigid ratio at $H = 5$ kft
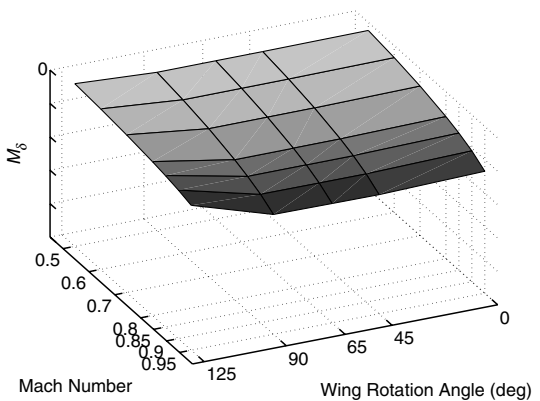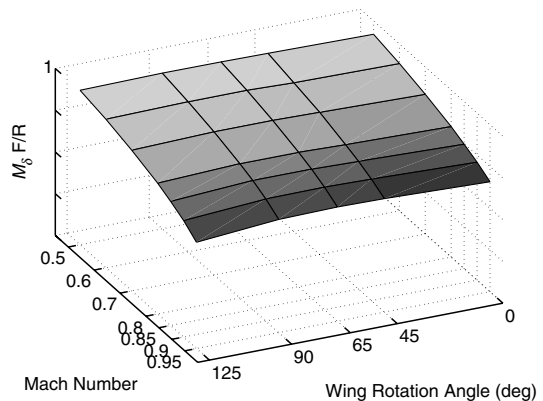
g) M_δ at $H = 30$ kft

h) Flexible-to-rigid ratio at $H = 30$ kft

Fig. 7   static aeroelastic dimensional control derivatives Z_δ and M_δ as a function of the Mach number and wing rotation angle χ.

$$P(\sigma) := \begin{bmatrix} A(\sigma) & B(\sigma) \\ C(\sigma) & D(\sigma) \end{bmatrix} \tag{7}$$

and the state-space description of the LPV system $P(\sigma)$ will range in a polytope of matrices whose vertices are the images of the vertices $\sigma_1, \sigma_2, \ldots, \sigma_N$, that is,

$$\begin{bmatrix} A(\sigma) & B(\sigma) \\ C(\sigma) & D(\sigma) \end{bmatrix} \in \mathrm{Co}\left\{ \begin{bmatrix} A_i & B_i \\ C_i & D_i \end{bmatrix} \right.$$
$$:= \left. \begin{bmatrix} A(\sigma_i) & B(\sigma_i) \\ C(\sigma_i) & D(\sigma_i) \end{bmatrix}, i = 1, \ldots, N \right\} \tag{8}$$

The combination of Eqs. (6) and (8) allows the $A(\sigma)$ matrix of $P(\sigma)$ to be written as

$$A(\sigma) = \sum_{i=1}^{N} \gamma_i A_i$$

For a generic parameter-dependent system matrix $X(\sigma) \in \mathbb{R}^{p \times p}$, the last affine matrix means that

$$\begin{bmatrix} x_{11} & \cdots & x_{1p} \\ \vdots & \ddots & \vdots \\ x_{p1} & \cdots & x_{pp} \end{bmatrix} = \sum_{i=1}^{N} \gamma_i \begin{bmatrix} x_{11_i} & \cdots & x_{1p_i} \\ \vdots & \ddots & \vdots \\ x_{p1_i} & \cdots & x_{pp_i} \end{bmatrix} \tag{9}$$

where each element $\{x_{jk}\}$ of $X(\sigma)$ is obtained as an affine linear combination of elements $\{x_{jk}\}_i$ weighted by the same coefficient γ_i. This can be recast into an estimation problem using a new vector $\mathbf{x}$, obtained by stacking the columns of $X(\sigma)$ on top of each other,

$$\mathbf{x} = [x_{11}, \ldots, x_{p1}, \ldots, x_{1p}, \ldots, x_{pp}]^T \tag{10}$$

and taking values within a convex hull defined by the vertices $\mathbf{x}_i = (x_{11_i}, \ldots, x_{p1_i}, \ldots, x_{1p_i}, \ldots, x_{pp_i})$, that is,

$$\mathbf{x} \in \mathrm{Co}\{\mathbf{x}_1, \ldots, \mathbf{x}_N\}$$

Using Eq. (6), it can be formulated as,

$$\begin{bmatrix} x_{11} \\ \vdots \\ x_{p1} \\ \vdots \\ x_{1p} \\ \vdots \\ x_{pp} \end{bmatrix} = \sum_{i=1}^{N} \gamma_i \begin{bmatrix} x_{11_i} \\ \vdots \\ x_{p1_i} \\ \vdots \\ x_{1p_i} \\ \vdots \\ x_{pp_i} \end{bmatrix} \tag{11}$$

Equation (11) states that, for the morphing elastic UAV model, the dimensional aeroelastic stability vector ρ is composed by the elements of the parameter-dependent system matrix $A(\sigma)$. In addition, it should be noted that each vector ρ_i is directly related to a particular LTI model generated for any one of the $N = n_f \times c_m$ operating points of the morphing UAV (MUAV). Clearly, the dimension of vectors ρ_i, that is, $\rho_i \in \mathcal{R}^5$, is given by the number of stability derivatives that compose the state-space description at each of the N vertices or extreme points [see Eq. (12)].

Hence, by using the small convex hull approach, the conservatism of the morphing LPV model will be greatly reduced. To reduce even further the number of vertices for the design, an additional criteria was also applied. Here, a subset of operating points from the set of the small hull's extreme values was selected by comparing them with the flight conditions that are of particular interest and most likely in accordance with the mission requirements.

By considering the smoother gradient variation of the aeroelastic control derivative Z_δ previously mentioned, a four-dimensional vector $\rho_i \in \mathcal{R}^4 = [Z_\alpha, M_\alpha, M_q, M_\delta]_i^T, i = 1, N$ was assumed.

Table 1 Extreme points selection approach

Iteration no.	Criteria	Extreme points
First round	Coarse mission requirements	143
Second round	Small convex hull concept	65
Third round	Most likely flight profile	11

Table 1 shows the number of flight conditions achieved using the proposed vertex reduction procedure. The first iteration round is obtained by considering only the flight conditions related to the fully extended ($\chi = 0$ deg, 70 operating points), and fully morphed ($\chi = 125$ deg, 70 operating points) configurations, plus the additional three morphing transition states, that is, $\chi = 45, 65,$ and 90 deg at some specific flight condition. Then, the total number of flight conditions is reduced to 143.

The second round involves the application of the proposed convex modeling concepts throughout the small convex hull algorithm. Specifically, the total number of extreme points that defines the convex hull for the coarse set of operating conditions is 65. Finally, an additional refinement is obtaining by considering the most interesting/likely flight conditions from the extreme points of the small convex hull. Hence, nine flight conditions are extracted from the small convex hull, plus two additional flight conditions that lie inside it.

C. Morphing Unmanned Aerial Vehicle Longitudinal Dynamics

Figure 8 schematically depicts the main components of the nominal $G_{\mathrm{MUAV}}(s)$ plant. The longitudinal dynamics were characterized using a two-state morphing UAV model that represents the short-period dynamics. Here, the main variables are the angle of attack $\alpha(t)$ and the pitch rate $q(t)$. A perturbation to the state dynamics is sought by w_g, coming from vertical gust activity.

$$\begin{bmatrix} \dot{\alpha} \\ \dot{q} \end{bmatrix} = \begin{bmatrix} Z_\alpha/U_0 & 1 \\ M_\alpha & M_q \end{bmatrix} \begin{bmatrix} \alpha \\ q \end{bmatrix} + \begin{bmatrix} Z_{\delta_e}/U_0 \\ M_{\delta_e} \end{bmatrix} \delta_e + \begin{bmatrix} -Z_\alpha/U_0 \\ -M_\alpha \end{bmatrix} \alpha_g \tag{12}$$

In addition, the output variables are

$$z = W_n(s) e_{a_n} (\text{weighted error}), \qquad y = \begin{bmatrix} q \\ \alpha_f \\ a_n \end{bmatrix} (\text{output signal})$$

where a_n is the normal acceleration sensed at the location x_a ahead of the morphing UAV's center of gravity, and α_f is a filtered version of the angle-of-attack variable $\alpha(t)$. The plant is shaped through the filters $W_{\mathrm{act}}(s)$ and $W_\alpha(s)$, both being representatives of common actuator and filter sensor elements used in actual flight control systems. The flaperon limits are ± 15 deg.

Note that the morphing's longitudinal dynamics change considerably during the one-minute time frame assumed to perform a morphing change of state. Equations (13–17) display the gain, pole, and zero configurations at each of the vertex plants for the specific morphing transformation. At the fully extended configuration, $V_5(\chi = 0$ deg), the normal acceleration transfer function presents an unstable pole ($p_1^{(5)}$), as well a nonminimum-phase zero ($z_1^{(5)}$), whereas, at the end of the morphing sequence, $V_9(\chi = 125$ deg), it is transformed into a stable and minimum-phase transfer function with
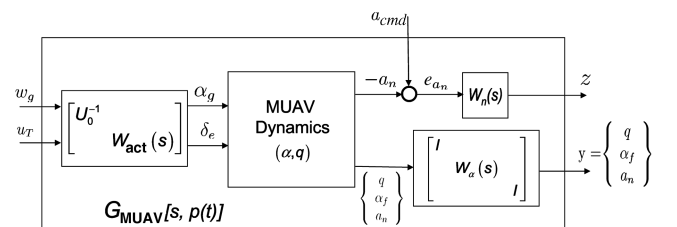

Fig. 8 Weighted longitudinal dynamics LPV plant.

complex-conjugate poles.

$$\frac{a_n}{\delta_e}(s)\Big|_{V_5} = \frac{k_5\left(s - z_1^{(5)}\right)\left(s + z_2^{(5)}\right)}{\left(s - p_1^{(5)}\right)\left(s + p_2^{(5)}\right)} \tag{13}$$

$$\frac{a_n}{\delta_e}(s)\Big|_{V_6} = \frac{k_6\left(s - z_1^{(6)}\right)\left(s + z_2^{(6)}\right)}{\left(s - p_1^{(6)}\right)\left(s + p_2^{(6)}\right)} \tag{14}$$

$$\frac{a_n}{\delta_e}(s)\Big|_{V_7} = \frac{k_7\left(s - z_1^{(7)}\right)\left(s + z_2^{(7)}\right)}{\left(s + p_1^{(7)}\right)\left(s + p_2^{(7)}\right)} \tag{15}$$

$$\frac{a_n}{\delta_e}(s)\Big|_{V_8} = \frac{k_8\left(s - z_1^{(8)}\right)\left(s + z_2^{(8)}\right)}{\left(s + p_1^{(8)}\right)\left(s + p_2^{(8)}\right)} \tag{16}$$

$$\frac{a_n}{\delta_e}(s)\Big|_{V_9} = \frac{k_9\left(s + z_1^{(9)}\right)\left(s + z_2^{(9)}\right)}{\left(s + p_1^{(9)}\right)\left(s + p_2^{(9)}\right)} \tag{17}$$

III.   Multiloop Controller Design Approach

The devised controller used a set of inner-loop gains to provide stability, as well as tracking performance characteristics at each of the selected extreme point/flight conditions for the aeroelastic morphing UAV. The outer loop is composed of an LPV controller with prescribed pole locations to guarantee a specific level of robust stability and performance, as well as solving the time-varying nature of the problem. Specifically, the general idea of separating the controller into two loops as shown in Fig. 9a, inner and outer, is as follows:

1) The inner controller $\{K_1(s), K_2\}$ is designed with traditional methods routinely used by flight control engineers. In particular, the linear quadratic (LQ) output feedback approach is suggested [6].
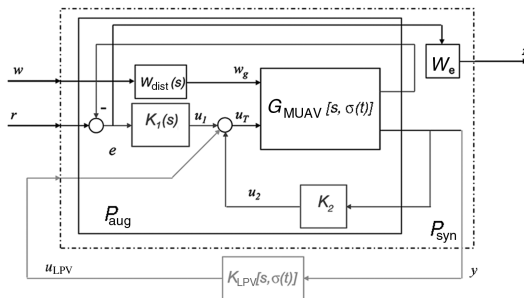
a) G_{MUAV}, Augmented model P_{aug} for simulation, and augmented model P_{syn} for controller design
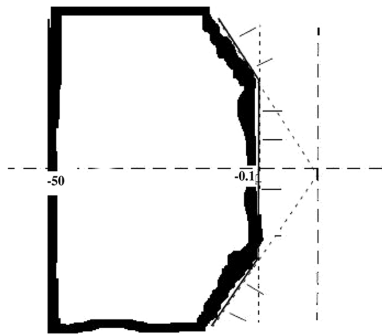
b) Pole placement region

Fig. 9   Longitudinal LPV model and closed-loop pole placement region.

This is a useful starting point to provide a nominal controller based on experience that can, at least, stabilize each flight condition separately, and provides a "nominally" stable multimodel system, that is, LTI stability *only* at each vertex. This does not guarantee quadratic stability of the time-varying underlying model.

2) The outer loop's LPV controller K_{LPV} is designed to cope with the time-varying LPV system to a) guarantee global quadratic stability of the system for fast flight condition transitions, in cases the previous multimodel nominal controller does not, and b) provide better performance in cases where the inner-loop does not provide reasonable results.

In addition, note that, independent of the time-varying nature of the problem, controlling this set of models described by the convex combination of all extreme LTI models (vertices) already provides robust stability and performance against uncertainty due to (slow) transitions between flight conditions, a consequence of the underlying nonlinear system.

3) Another advantage of the LPV design is that a careful selection of weights could provide a better (suboptimal) robust performance. These weights are well understood among the flight control community and they are related to well-defined loop variables, for example, control action, tracking error, etc., and have been extensively used in $\mathcal{H}_\infty$ optimal control design [7,8].

4) In the design, care will be taken to avoid "fast poles" in the LPV controller by adding a pole placement (linear matrix inequality) constraint, as depicted in Fig. 9b. Also, the order of each individual vertex controller will be kept to a minimum to favor implementation.

Figure 9a presents the model interconnection, which is used both for controller design (P_{syn}) and for simulation (P_{aug}). The autopilot's command or reference $r(t)$, as well as the disturbances $w(t)$, are modeled as part of the design. The latter can be sought as the Dryden second-order gust model. Both the plant and the controller are updated by means of a parameter $\sigma(t)$, which is measured in real time. In addition, it illustrates the signals from the inner ($u_1 + u_2$) and outer (u_{LPV}) controllers, which add up to $u_T = u_1 + u_2 + u_{LPV}$. Its relation with the flaperon deflection angle δ_e is defined in Fig. 8 through the actuator dynamics $W_{act}(s)$, that is, $\delta_e = W_{act}(s)u_T$.

A.   Linear Quadratic Output Feedback Inner-Loop Controller

The inner-loop gains are designed closely following the approach presented by Stevens and Lewis [6]. Figure 10 depicts the inner-loop setup. Assuming that the morphing UAV dynamics are given by

$$\dot{x}_p = A_p x_p + B_p u_p \tag{18}$$

$$y_p = C_p x_p \tag{19}$$

where x_p, u_p, and y_p are the state, input, and measured output vectors, respectively. The performance output $z = H_p x_p$ should track the reference signal r and the closed-loop system's tracking error is $e = r - z$. The compensator with the prescribed structure is described by

$$\dot{x}_c = A_c x_c + B_c e \tag{20}$$

$$y_p = C_c x_c + D_c e \tag{21}$$

where x_c and v are the controller state and output vectors. The morphing plant input is
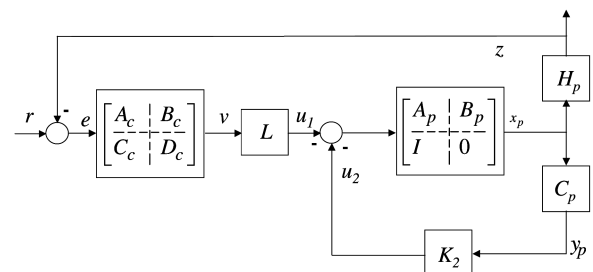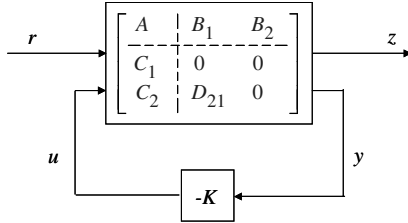

Fig. 10   Inner-loop setup.

Fig. 11   LQ output feedback setup.

$$u = -\underbrace{\begin{bmatrix} K_2 & L \end{bmatrix}}_{K} \begin{bmatrix} y_p \\ v \end{bmatrix} \qquad (22)$$

where the constant gains K_2 and L are selected to satisfy some predefined closed-loop requirements.

Next, by defining augmented state and output vectors, $x = \begin{bmatrix} x_p^T & x_c^T \end{bmatrix}^T$ and $y = \begin{bmatrix} y_p^T & v^T \end{bmatrix}^T$, the dynamics of the morphing plus inner-loop compensator are shown in Fig. 11 and described by

$$\dot{x} = Ax + B_1 r + B_2 u \qquad (23)$$

$$y = C_2 x + D_{21} r \qquad (24)$$

$$z = C_1 x \qquad (25)$$

with y as the measured output and z as the performance output that tracks r.

Note from Fig. 11 that the input to the augmented plant is $u = -Ky$, with the output gain K being selected to guarantee stability as well as good tracking of the reference signal r. Therefore, to solve the output gain problem, Stevens and Lewis [6] devised the conversion from the tracking to a regulator problem, using a new set of deviation variables. Finally, to make the deviation error small, $\tilde{e}$ (small tracking error), the output gain K is selected to minimize the following time-weighted performance index:

$$J = \int_0^\infty (t^k \tilde{e}^T \tilde{e} + \tilde{u}^T R \tilde{u}) \qquad (26)$$

Observe that the presence of the term t^k in the performance index gives rise to an optimal time-variant gain K which minimizes J. Nevertheless, a time-invariant gain K is preferred, although achieving a suboptimal solution. Therefore, an algebraic optimization problem is solved numerically using an iterative procedure through a system of nested Lyapunov equations.

Figures 12a and 12b show the time traces of the closed-loop system, using the designed LQ inner-loop gains, for the five flight conditions involved in a complete morphing transformation, that is, from a fully extended to a fully morphed configuration. The plotted variables are the normal acceleration response a_n to $+1g$ step commands, as well as the required flaperon deflection angle δ_e. To synthesize these five inner-loop gains, only one parameter was moved along the LQ process. All normal acceleration responses are well behaved and the flaperon deflection angles are within limits (± 15 deg), except at vertex V_9. This issue was solved with the outer-loop morphing vertices V_5–V_9.

B.   Linear Parameter-Varying Outer-Loop Controller

Two practical facts should be considered here: the fast poles problem described before and the controller order at each "extreme" point of the variation region.

1) The problem of fast poles for LTI models is handled by using closed-loop pole placement linear matrix inequality (LMI) regions in the design phase [9]. The LMI region has been illustrated in Fig. 9b. Here, an upper bound in the real part of the closed-loop (frozen) poles (see footnote ¶ on p. 1687) as well as damping limits have been adopted. This approach considers a general LMI region defined as follows:
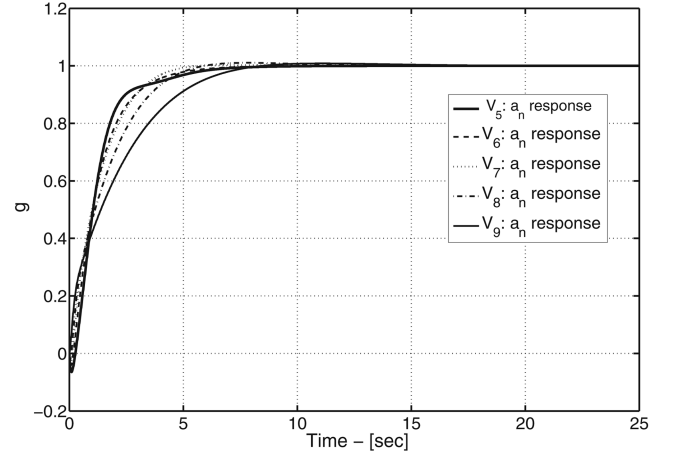
a) Inner-loop tracking normal acceleration command
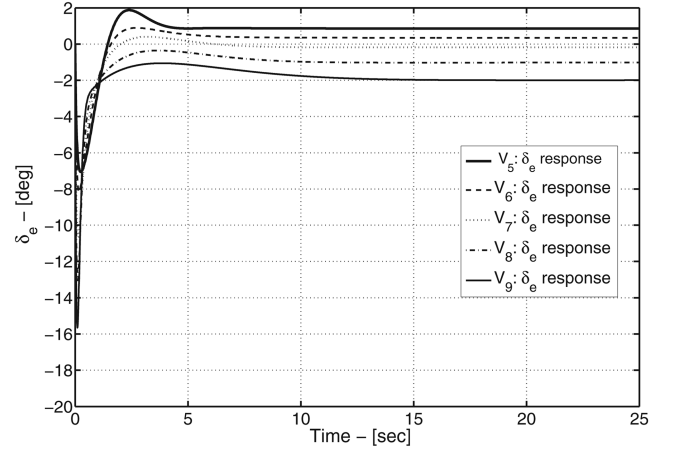
b) Inner-loop elevator responses

Fig. 12   Inner-loop controller performance.

Definition 1: A subset $\mathcal{D}$ of the complex plane is called an LMI region if there exists a symmetric matrix $\alpha = [\alpha_{k\ell}] \in \mathbb{R}^{m \times m}$ and a matrix $\beta = [\beta_{k\ell}] \in \mathbb{R}^{m \times m}$ such that $\mathcal{D} = \{z \in \mathbb{C}: f_\mathcal{D}(z) < 0\}$ with

$$f_\mathcal{D}(z) = \alpha + z\beta + \bar{z}\beta^T = [\alpha_{k\ell} + \beta_{k\ell}z + \beta_{\ell k}\bar{z}]_{1 \le k, \ell \le m} \qquad (27)$$

A matrix $A \in \mathbb{R}^{n \times n}$ is $\mathcal{D}$ stable if and only $\exists X_\mathcal{D} > 0$:

$$\alpha_{k\ell} X_\mathcal{D} + \beta_{k\ell} A X_\mathcal{D} + \beta_{\ell k} X_\mathcal{D} A^T < 0 \qquad 1 \le k, \ell \le m$$

The analysis result guarantees that a controller that provides quadratic stability and $\mathcal{H}_\infty$ performance, as well as the "pole placement" properties described before, just adds a finite set of LMIs, whose number depends on the size of the function $f_\mathcal{D}(z)$ used to describe the LMI region. Hence, for practical computational reasons, these regions are selected as simple as possible, as the one used in this case.

As a consequence, closed-loop matrices A_cl, B_cl, C_cl, and D_cl achieve $\mathcal{D}$ stability and $\|T_{zw}\|_\infty < \gamma$ if there exist matrices $X_\infty > 0$ and $X_\mathcal{D} > 0$ such that

$$\begin{bmatrix} A_\mathrm{cl}^T X_\infty + X_\infty A_\mathrm{cl} & X_\infty B_\mathrm{cl} & C_\mathrm{cl}^T \\ B_\mathrm{cl}^T X_\infty & -\gamma I & D_\mathrm{cl}^T \\ C_\mathrm{cl} & D_\mathrm{cl} & -\gamma I \end{bmatrix} < 0 \qquad (28)$$

$$\begin{bmatrix} \alpha_{k\ell} X_\mathcal{D} + \beta_{k\ell} A_\mathrm{cl} X_\mathcal{D} + \beta_{\ell k} X_\mathcal{D} A_\mathrm{cl}^T \end{bmatrix} < 0 \quad \text{for all } 1 \le k, \ell \le m$$
$$(29)$$

In the LPV case, these poles exist only at frozen times, due to the time-varying nature of the model. Nevertheless, from a practical

point of view, the previous pole placement results have been successfully extended [10,11] to LPV applications. There, the LMI regions limit the fast poles that are generated in LPV controller design with single Lyapunov functions, which include infinitely fast parameter variations.

As mentioned previously, the set of models described by the convex combination of all extreme LTI models (vertices) also represents a system which, independent of its time variation, describes the uncertainty due to (slow) transitions between flight conditions. Providing performance and stability to the whole multimodel set illustrates the robustness of this design.

2) Controller order:

a) As usual, the order of the resulting controller is kept to a minimum due to practical real-time implementation issues. The fact that the LQ-based inner-loop controller is designed as a starting point produces a low-order controller already. This controller is in line with what is used in standard aeronautical applications.

b) The outer-loop controller is there to guarantee time-varying quadratic stability and robust performance. Its order at each extreme point of the polytopic region of parameter variations depends on the order of the nominal plant model and the stability and performance weights. Hence, these weights are designed with the minimum possible order, as a general rule, and, if possible, as constant values.

The advantage of this methodology of separating inner- and outer-loop designs is based on combining very practical approaches. On one hand, the available knowledge of aeronautical engineers involved in more standard applications is used in the inner-loop design. On the other hand, the efficient LMI-based computations provide the necessary guarantees of quadratic stability and performance due to the LPV outer-loop controller, which will presumably reduce the amount of testing and simulations.

IV. Controller Model Reduction: Coprime Factor Approach

In this section, the design of the reduced controller via model order reduction of a coprime factor representation of the synthesized full-order controller is proposed. The reduction will be applied on the higher-order outer-loop LPV controller, given that the inner-loop is built upon a proportional/integral controller. A practical but effective approach to reduce the LPV model order is adopted, although other methods could also be applied [12]. Here, each controller vertex is reduced by this method, thus keeping track of the orders among that them are similar. Next, a verification step to test the distance between the full- and reduced-order controller using the ν gap is applied.

A major difficulty in reducing the controller degree is to ensure that the reduction error does not adversely affect closed-loop objectives. Specifically, these objectives are related with the time response behavior of the parameter-dependent closed-loop system, as well as the location of the resulting closed-loop poles using the reduced-order controllers. Generally, the objective of any closed-loop model reduction is to generate a reduced-order controller which stabilizes a given extreme nominal plant.

The achieved outer-loop controllers have nine states at each extreme condition. By applying the proposed balanced reduction technique to its normalized right coprime factor representation [13], these are reduced to six states. To assess the impact of the reduction process on the closed-loop stability, the so-called ν-gap value is computed between the full-order controller and the reduced-order controller. Note that, the approximation in the ν-gap metric is appealing because the ν gap between two open-loop systems is a measure of the maximum possible difference in closed-loop behavior. For the morphing UAV concept, a ν gap numerically near to zero was achieved for each extreme point controller when the controller dimension was reduced from nine to six states.

By comparing the full- and reduced-order controller eigenvalues for the morphing sequence, going from vertex V_5 to V_9, it was observed that, in general, the lower-frequency behavior is fully

preserved, although some high-frequency complex-conjugate poles move to higher-frequency locations.

V. Simulations

The full- and reduced-order multiloop controllers are evaluated through the same parameter trajectories, that is, simultaneous morphing configuration and acceleration changes. These controllers include both the inner-loop and the outer LPV controllers. The actual time-varying physics are simulated, which include the state morphing transformation through the time-varying parameter simultaneously with the normal acceleration reference command.

Two maneuvers are sought to exhaustively evaluate the performance of the synthesized multiloop controller, subject to large-scale geometrical changes. In addition, it was assumed that the out-of-plane morphing shape change will be slowly varying, that is, approximately between 30 s and 1 min. Hence, the devised maneuvers will consist of tracking a predefined, slightly ramped acceleration doublet, of the same duration, while performing a variety of out-of-plane morphing transformations.

Figures 13 and 14 depict the devised normal acceleration commands as well as the programmed in-flight morphing configuration sequences for maneuver numbers 1 and 2, respectively. It can be observed that the complete large-scale morphing transformation is involved along these maneuvers. The UAV presents a fully extended configuration at the beginning of the maneuver, changing to another state before reaching the uphill ramp segment. Once the reference $+1g$ acceleration value is achieved, one or two in-flight configuration changes are executed. Finally, the downhill ramp segment is followed by another morphing state until the steady flight condition is reached again.

This cycle is repeated again but now by following a negative acceleration command $(-1g)$. Specifically, Fig. 13 represents a $\chi = 45$ deg wing inboard angle configuration ramped up until $+1g$ is reached, a switch to $\chi = 65$ deg and then to $\chi = 90$ deg to follow the ramped down command, and finally it morphs to $\chi = 125$ deg. On the other hand, Fig. 14 indicates a more complex morphing sequence also described by the self-included table.

In what follows, full-line traces represent closed-loop systems with the full-order controller K_{full}, whereas dashed traces are used to indicate the results achieved using the reduced-order controller K_{red}.

Figure 15a shows the responses of normal acceleration a_n, pitch rate q, normal acceleration error e_{a_n}, and flaperon deflection angle δ_e to the acceleration command. This plot indicates a very close match between the main variables used to describe the performance of both closed-loop systems, except for the elevator deflection plot at $t = 70$ s. Figure 15b provides a closer detail on the control action spike, depicted on the lower-right corner subfigure of Fig. 15a, that occurs at that particular instant in time.

Figures 16a and 16b show similar dynamic behaviors for maneuver number 2 (see Fig. 14), again with a slight difference between full- and reduced-order controllers at time $t = 70$ s.

For both maneuvers, the reduced-order controller performs well along the selected maneuver profiles, although it presents some slight performance degradation when the inboard morphing angle changes
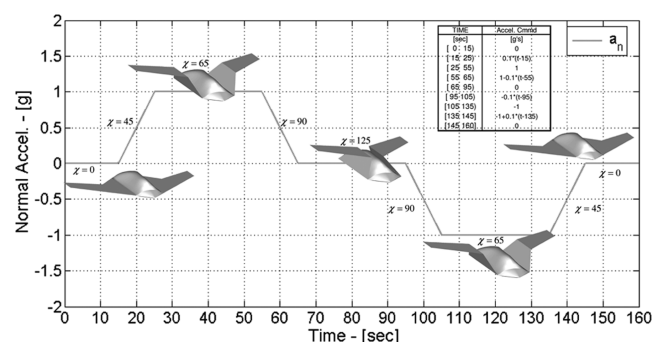

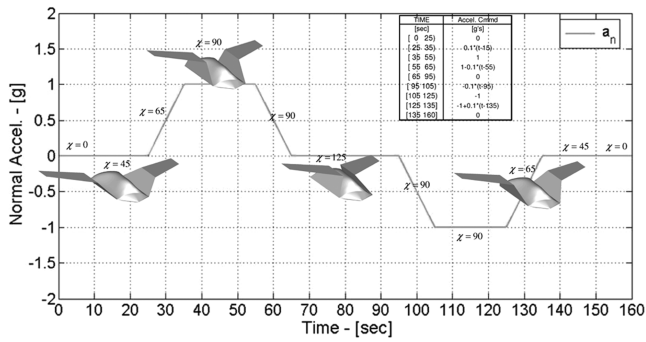**Fig. 13 Tracking a doublet acceleration command with in-flight morphing sequence no. 1.**

Fig. 14 Tracking a doublet acceleration command with in-flight morphing sequence no. 2.

from $\chi = 90$ deg to $\chi = 125$ deg. Presumably, this deteriorated closed-loop system behavior could be related to the presence of the higher-frequency complex-conjugate poles that consistently appear during the reduction process, as indicated before.

The closed-loop system LPV (frozen) poles for both maneuvers, shown in Fig. 17 for the full-order controller (as asterisks), are satisfactorily located in the prescribed region illustrated in Fig. 9b, using the proposed LPV technique with pole placement. On the other hand, the coprime factor reduction approach clearly shows that a tradeoff needs to be achieved between the controller's order reduction and the achieved high-frequency pole locations (circles in Fig. 17). In spite of this, both full- and reduced-order controllers can be implemented with a nominal sampling rate between 40 and 80 Hz, as could be the case in standard flight controller implementation.
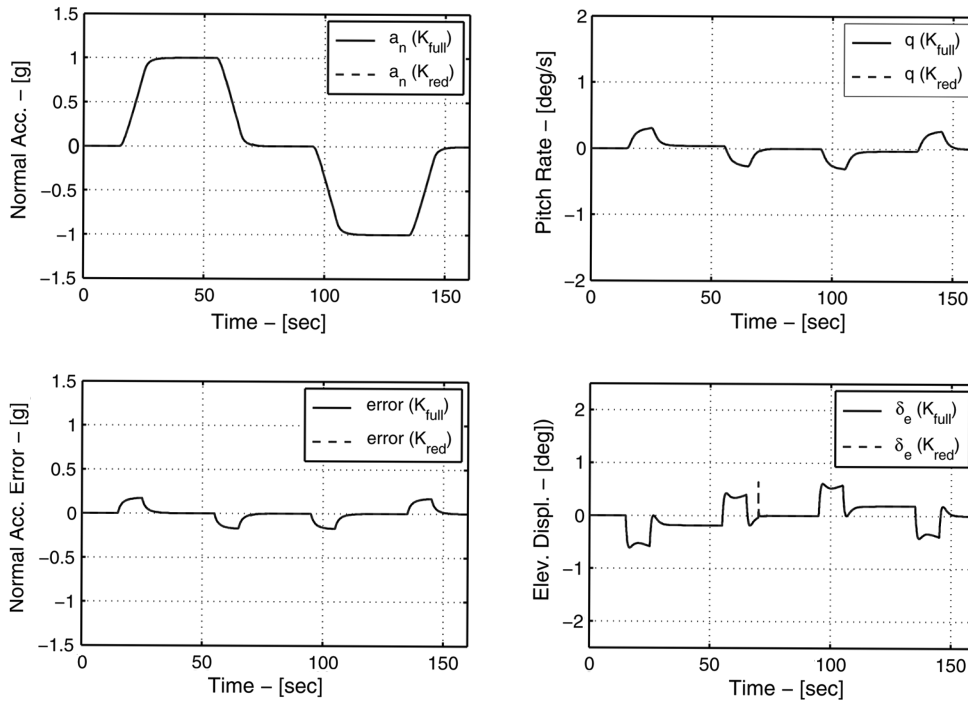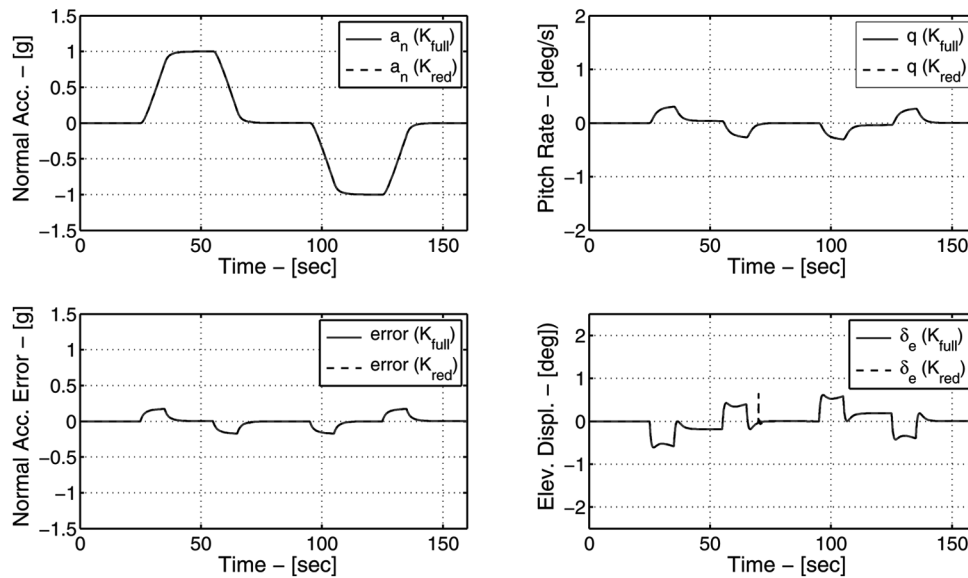

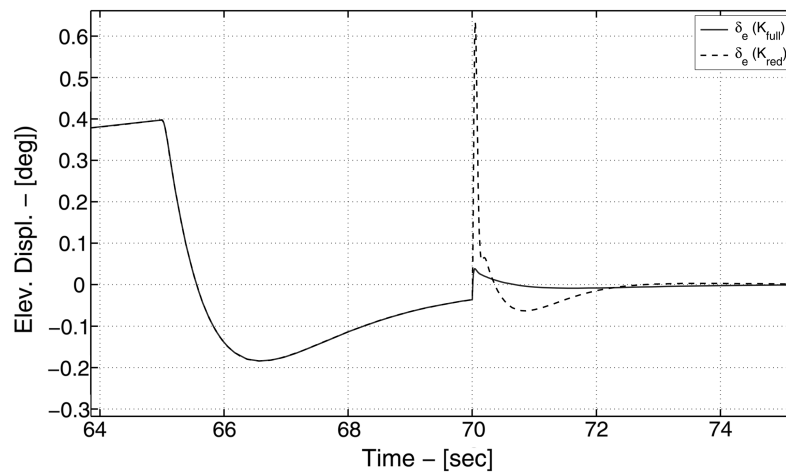**a) Tracking normal acceleration command: main variables**
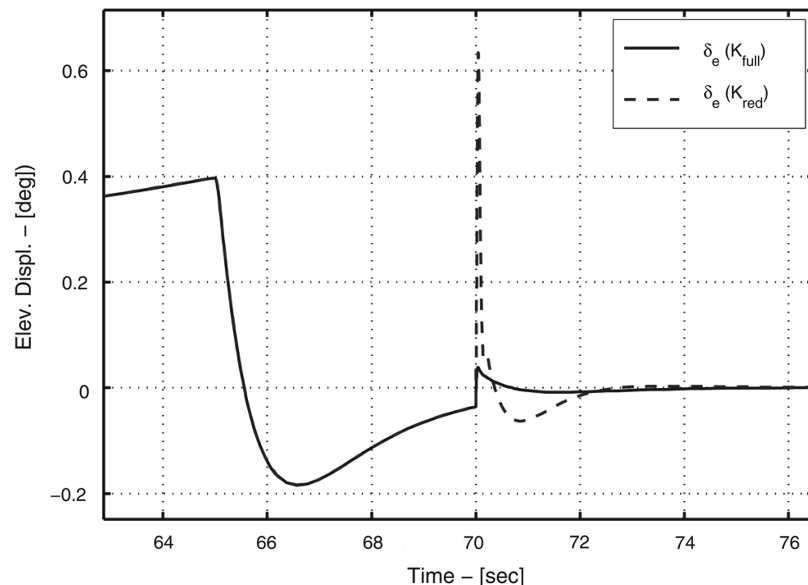
b) Control action difference (zoom of peak in previous figure)

Fig. 15 Multiloop controller performance (maneuver no. 1).

a) Tracking normal acceleration command: main variables

b) Control action difference (zoom of peak in previous figure)

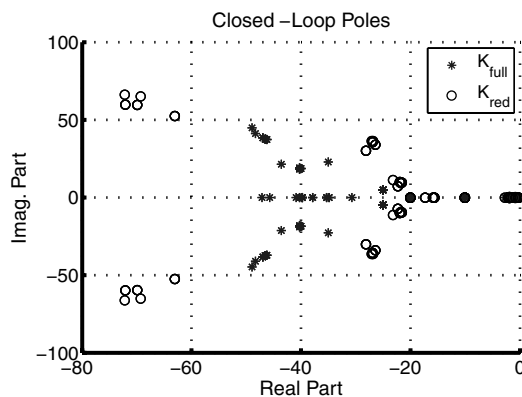Fig. 16   Multiloop controller performance (maneuver no. 2).

Fig. 17   Closed-loop locations: full- vs reduced-order controllers.

VI.   Conclusions

Based on these preliminary results, it was found that the underlying multiloop approach, using the LPV with pole placement technique, can properly account for efficient in-flight transformation between vehicle states in less than 1 min, while maintaining the overall vehicle stability and control. During this work, it was assumed that the morphing UAV behaves as a variable geometry rigid body, although the dynamic coefficients used in the differential equations were corrected for quasi-steady aeroelastic effects. To this end, the dimensional stability and control derivatives were modified by flexible-to-rigid ratios. A total of 350 operating points were computed by considering a generic morphing UAV mission profile. Based on these flight conditions, a rather extensive set of aeroelastic dimensional stability and control derivatives were generated.

By applying the small convex hull approach in conjunction with the most likely flight conditions that result from its own set of extreme points, the conservatism of the morphing LPV model was consistently reduced within the convex modeling framework. In this way, a reduced set composed of 11 extreme points/flight conditions was achieved.

By exploiting the multiloop topology, a practical LPV controller was designed to perform in-flight large-scale geometrical changes while tracking a predefined acceleration command. The proposed controller uses a set of inner-loop gains to provide stability and some level of performance to the intrinsic unstable morphing UAV dynamics, whereas the outer-loop LPV controller guarantees global quadratic stability of the time-varying system. The full-order multiloop controller had 10 states: one state for the inner-loop and the

remaining nine for the outer-loop controller. A reduced-order controller was synthesized using balance model reduction of its normalized coprime factor realization. The achieved reduced-order multiloop controller presented a total of only seven states.

Acknowledgments

References

[1] Wall, R., "Taking Shape," *Aviation Week and Space Technology*, 5 Jan. 2004, pp. 54–56.

[2] Rough, W. J., and Shamma, J. S., "Research on Gain Scheduling," *Automatica*, Vol. 36, No. 10, 2000, pp. 1401–1425.
doi:10.1016/S0005-1098(00)00058-3

[3] Kumar, A., and Anderson, M. R., "Comparison of LPV Modeling Techniques for Aircraft Control," *AIAA Guidance, Navigation, and Control Conference and Exhibit*, AIAA Paper 2000-4458, 2000, pp. 1534–1543.

[4] Smetana, F. O., *Computed Assisted Analysis of Aircraft: Performance, Stability & Control*, McGraw–Hill, New York, 1984, pp. 5–163.

[5] "ZAERO User's Manual," Ver. 8.2, ZONA Technology, Scottsdale, AZ, June 2007.

[6] Stevens, B. L., and Lewis, F. L., *Aircraft Control and Simulation*, 2nd ed., Wiley, New York, 2003.

[7] Zhou, K., Doyle, J. C., and Glover, K., *Robust and Optimal Control*, 1st ed., Prentice–Hall, Upper Saddle River, NJ, 1996, pp. 449–495.

[8] Sánchez Peña, R. S., and Sznaier, M., *Robust Systems Theory and Applications*, 1st ed., Wiley, New York, 1998, pp. 61–125.

[9] Chilali, M., and Gahinet, P., "$\mathcal{H}_\infty$ Control Design with Pole Placement Constraints: An LMI Approach," *IEEE Transactions on Automatic Control*, Vol. 41, No. 3, March 1996, pp. 358–367.
doi:10.1109/9.486637

[10] Ghersin, A. S., and Sánchez Peña, R. S., "Transient Shaping of LPV Systems," *European Control Conference 2001, Invited Paper*, Porto, Portugal, 2001.

[11] Ghersin, A. S., and Sánchez Peña, R. S., "LPV Control of a 6-DOF Vehicle," *IEEE Transactions on Control Systems Technology*, Vol. 10, No. 6, Nov. 2002, pp. 883–887.
doi:10.1109/TCST.2002.804123

[12] Lall, S., and Beck, C., "Error-Bounds for Balanced Model-Reduction of Linear Time-Varying Systems," *IEEE Transactions on Automatic Control*, Vol. 48, No. 6, 2003, pp. 946–956.
doi:10.1109/TAC.2003.812779

[13] McFarlane, D. C., Glover, K., and Vidyasagar, M., "Reduced-Order Controller Using Coprime Factor Model Reduction," *IEEE Transactions on Automatic Control*, Vol. 35, No. 3, March 1990, pp. 369–373.
doi:10.1109/9.50362